Optimal Control of Multiphoton Excitation: A Black Box or a Flexible Toolkit?

Ignacio R. Sola,[†,‡] Jesus Santamaria,[†] and David J. Tannor*[,‡]

Departamento de Quimica Fisica, Universidad Complutense de Madrid, Spain, and Chemical Physics Department, Weizmann Institute of Science, Rehovot, Israel

Received: November 20, 1997; In Final Form: February 18, 1998

Optimal control theory (OCT) applied to driving molecular systems by means of femtosecond pulses is now a mature area, but many of its intricacies are as yet unexplored. As a numerical tool, the many variations on the basic method differ not only in computer efficiency but in the type of solutions obtained. In this paper we survey this diversity, focusing on the use of multiphoton IR laser excitation to control either (1) the state selectivity or (2) the photodissociation in a 1D Morse potential. We compare two distinct algorithms, the Krotov method and the gradient method. The former method generates large changes in the field at each iteration, while the latter does not. As a result, the Krotov method virtually always leads to pulses that are very different from the initial guess, while with the gradient method this is not always the case. We then analyze the effect of changing the final time, *T*, and find that it also can have a profound effect on the nature of the optimal solutions. Finally, we compare the solutions obtained using two different projectors to describe the bond-breaking process: a coordinate projector and a projector over scattering states. Again we observe that the optimal pulses and the dynamics they generate are markedly different in the two cases. This ambiguity in the definition of the optimal pulses may be viewed as a shortcoming of the approach, or alternatively it may be viewed as giving the method extra flexibility.

I. Introduction

In the last few years great progress has been made, both experimentally and theoretically, in observing and controlling molecular motion. Using femtosecond laser fields, it is possible to control both the time delay[1] and the relative phase between pump and probe pulses[2] to clock chemical reactions and to probe the detailed evolution of wavepacket amplitude. With newly developed pulse-shaping techniques,[3,4] it has become possible to control both the amplitude and phase of femtosecond pulses at each component frequency and to update at a high repetition rate. Very recently there have been reports of successful control in simple systems[5,6] using both time-dependent and time-independent mechanisms.

An outstanding goal of this effort at molecular control is to learn to use laser light to selectively break chemical bonds. Many attempts in the 1960s to use strong fields/multiphoton excitation in the IR to dissociate diatomics were unsuccessful. In small molecules, with a low density of states, it was found that with the available field strengths it was not possible to overcome the anharmonicity in the potential and to reach dissociation. In larger molecules, although the density of states was much higher, intramolecular vibrational energy redistribution (IVR) was so fast that the dissociation fragments were statistical. Starting in the mid-1980s several imaginative schemes were proposed to produce high vibrational excitation/dissociation in diatomics at moderate field strengths. Paramonov and co-workers[7] developed a scheme to produce vibrational excitation using a fundamental frequency with satellite bands. Bandrauk[8] showed how a properly matched chirped excitation could lead to high vibrational excitation and significant amounts of dissociation. Rabitz[9] and co-workers applied techniques of optimal control theory to this problem and also found successful preparation of highly excited vibrational states.

In this paper, we reexamine the use of OCT for selective excitation in molecules. Although the use of OCT for controlling molecular motion is now well established and illustrations in the literature abound, there are still many aspects of its use that are not completely understood. As a numerical tool, the many variations possible differ not only in computer efficiency but in the type of solutions obtained. In this paper we survey this diversity, focusing on the use of multiphoton IR laser excitation to control either (1) the state selectivity or (2) the photodissociation in a 1D Morse potential. We compare two distinct algorithms, the Krotov method (KM) and the gradient method (GM). The former produces large changes in the field at each iteration, and hence has a propensity to generate optimal fields that are dramatically different from the initial guess. The latter makes comparatively small changes at each iteration and often the optimal field will be close in function space to the initial guess. Hence, the optimal fields obtained by the two methods may differ significantly. In addition, we analyze the effect of changing the final time *T*, which is a parameter in the optimization calculation. We find for different values of *T* dramatically different forms of the optimal field: for larger values of *T* the mechanism tends to be direct single-photon excitation to the target state, while for smaller values of *T* the mechanism is multiphoton excitation. Finally, we compare the optimal fields obtained using two different definitions of the projector to describe the bond-breaking process: a coordinate projector and a projector over scattering states. Again we observe that the optimal pulses and the dynamics they generate differ significantly, in a way that can be rationalized clearly.

Although not shown in the paper, we use the Husimi representation to analyze the time−frequency structure of the pulses. We find that all the pulses generated here consist of a time-independent electric field (dc component) along with

[†] Universidad Complutense de Madrid.
[‡] Weizmann Institute of Science.

S1089-5639(98)00281-3 CCC: $15.00
Published on Web 04/22/1998

Gaussian-shaped pulses of different colors, working essentially at the same time.

The paper is organized as follows. In section 2 we briefly describe the OCT equations arising from a full variational treatment,[9] and compare the GM and KM approaches. In section 3 we introduce the specific form for the Hamiltonian of the system under study. In section 4.1 we give the results of the numerical comparison of the methods, analyzing the distinct features of the pulses and striving to understand the physical mechanisms underlying the driven dynamics. In section 4.2 the effect of changing the final time is discussed, while in section 4.3 the effect of changing the dissociation projector is addressed. Section 5 is a Conclusion.

II. Methodology

In this section we briefly review Krotov's methodology and compare it with the more usual GM. To facilitate the comparison, we will adopt a unified nomenclature that follows closely that used in refs 9−11.

We start by defining the pieces that compose the functional J we want to maximize. First, we define the desired final state at a specified time T in terms of the expectation value of a projector,

$$\langle O(T)\rangle = \langle\psi(T)|\mathrm{O}\rangle\langle\mathrm{O}|\psi(T)\rangle \tag{1}$$

where $|\psi(T)\rangle$ is the system wave function at the final time and $|O\rangle$ the target state. This expectation value is the probability of being found in the desired state at time T, and we will refer to it as the objective functional. It is a functional in that it depends on the electric field at all earlier times.

To avoid the singularity of the equations, we add a term to the functional that depends explicitly on the field $\epsilon(t)$ to second order. A physically meaningful choice is to constrain the energy of the field by penalizing its intensity[11] in the form

$$\lambda\int_0^T \mathrm{d}t\, \epsilon^2(t) \tag{2}$$

where λ is a positive number that works as a penalty. Summing up the pieces, we have for the functional

$$J = \langle O(T)\rangle - \int_0^T \mathrm{d}t\, (\lambda\epsilon^2(t)) \tag{3}$$

Now we use a Lagrange multiplier technique to remove the dependence of the objective functional on the dynamical equations that govern the wavepacket evolution. This is done by defining a Lagrange multiplier function, $\chi(t)$, which multiplies the TDSE and generates the unconstrained functional $\bar{J}$. Following Krotov and Feldman,[12] we then split the time-dependent and time-independent parts of the functional and maximize them independently, arriving at the following formula.[11]

$$\bar{J} = G + \int_0^T R(t)\, \mathrm{d}t \tag{4}$$

with

$$G = \langle O(T)\rangle - (\langle\chi(T)|\psi(T)\rangle + \text{c.c.})|_0^T \tag{5}$$

$$R(t) = -\lambda\epsilon^2(t) + \left(\langle\dot{\chi}(t)|\psi(t)\rangle + \left\langle\chi(t)\left|\frac{H(\{\epsilon(t)\})}{\mathrm{i}\hbar}\right|\psi(t)\right\rangle + \text{c.c.}\right) \tag{6}$$

where c.c. stands for the complex conjugate and the dot represents a time derivative.

As in the usual variational procedure, we take now the differential of the functional with respect to variations in the unconstrained functions, $|\psi(T)\rangle$, $|\psi(t)\rangle$, and $\epsilon(t)$, up to first order, arriving at the set of equations

$$|\chi(T)\rangle = |O\rangle\langle O|\psi(T)\rangle \tag{7}$$

$$|\dot{\chi}(t)\rangle = \frac{H}{\mathrm{i}\hbar}|\chi(t)\rangle \tag{8}$$

$$\epsilon(t) = I\left(\left\langle\chi(t)\left|\frac{\mu}{\lambda\hbar}\right|\psi(t)\right\rangle\right) \tag{9}$$

The symbol I stands for the imaginary part. Equation 8 defines the equation of motion for $|\chi(t)\rangle$, which is seen to be identical to the TDSE for ψ. The boundary conditions for χ are specified at the *final* time, according to eq 7. The physical interpretation of this equation is that $\chi(T)$ is the part of ψ that has reached the objective.[10] The TDSE for both $|\psi(t)\rangle$ and $|\chi(t)\rangle$ are solved numerically using the split-operator algorithm with the Fourier grid method. The last equation, eq 9, is an equation for the optimal pulse. It is an implicit equation in the sense that the bra and ket themselves depend on the field, and therefore this equation needs to be solved iteratively. In GM we consider the functional derivative as a gradient.

$$\frac{\delta R}{\delta\epsilon(t)} \equiv \nabla_\epsilon R = 2\, I\left(\left\langle\chi(t)\left|\frac{\mu}{\lambda\hbar}\right|\psi(t)\right\rangle\right) - 2\lambda\epsilon(t) \tag{10}$$

and make $\epsilon_{k+1} = \epsilon_k + \alpha\nabla_\epsilon R$, where α is a parameter of line search and the subindex k refers to the iterative process. Instead of the gradient we could follow the conjugate gradient direction of the functional derivative with respect to the field, as in the conjugate gradient line-search method (CGM).

In contrast, in KM we do not assume infinitesimal steps, but take instead finite increments of the functions at each iteration. Following the derivation of Tannor et al.,[11] a specific form for the auxiliary function and optimal field is assumed in order to ensure that the increment in the functional is positive at each iteration. For the final time part,

$$\Delta G = G(\psi(T) + \Delta\psi(T)) - G(\psi(T)) = \langle\Delta\psi(T)|O\rangle\langle O|\Delta\psi(T)\rangle \geq 0 \quad \text{if} \quad |\chi(T)\rangle = |O\rangle\langle O|\psi(T)\rangle \tag{11}$$

which is exactly the result obtained using the GM. For the time-dependent part, defining

$$\Delta R = R(\psi(t) + \Delta\psi(t), \epsilon(t) + \Delta\epsilon(t)) - R(\psi(t) + \Delta\psi(t), \epsilon(t)) + R(\psi(t) + \Delta\psi(t), \epsilon(t)) - R(\psi(t), \epsilon(t)) = \Delta R_1(t) + \Delta R_2(t) \tag{12}$$

we have

$$\Delta R_2(t) = 0 \quad \text{if} \quad \langle\dot{\chi}(t)| = -\langle\chi|\frac{H}{\mathrm{i}\hbar} \tag{13}$$

$$\Delta R_1(t) = -\lambda(\Delta\epsilon)^2 - 2\lambda\epsilon\Delta\epsilon + \frac{2}{\hbar}\Delta\epsilon\, I\,(\langle\chi(t)|\mu|\psi(t) + \Delta\psi(t)\rangle) \tag{14}$$

which is a quadratic form in $\Delta\epsilon$ that takes a maximum, positive value for

$$\Delta\epsilon(t) = I\left(\left\langle\chi(t)\left|\frac{\mu}{\lambda\hbar}\right|\psi(t) + \Delta\psi(t)\right\rangle\right) - \epsilon(t) \tag{15}$$

When we collect all the terms into which we partitioned the functional and perform the time integral of $R(t)$, we find that $\Delta\bar{J} \geq 0$. The equality is attained only at the maximum, when we recover the forms of eqs 8−10.

From the variation in the field, eq 15, we calculate the new field $\epsilon_{k+1}(t) = \epsilon_k(t) + \Delta\epsilon_{k+1}(t)$, which according to formula 15 above does not depend on the former value, ϵ_k. Equation 15 resembles that for the variationally found optimal pulse, eq 9, except here the improved pulse ϵ_{k+1} is used to propagate the system wave function $(\psi(t) + \Delta\psi(t)\rangle)$, but not the auxiliary wave function, which is still propagated using the former version of the pulse ϵ_k. This procedure, where the pulse is optimized at each time step, is called immediate feedback control or local optimization.

From a different perspective, we observe that the Krotov method considers variations of the functional $\bar{J}$ up to second order in the field, and therefore we can calculate analytically the value of $\Delta\epsilon(t)$ which yields a maximum. Thus, the "empirical" test of the line-search approach is avoided in the Krotov method.[11]

From a computational point of view, the KM requires the following operations at each iteration: one backward propagation of $|\chi(t)\rangle$ and two forward propagations, one for $|\chi(t)\rangle$ driven by the old pulse and one for $|\psi(t)\rangle$ driven by the new pulse. In GM we need two backwards propagations, one for $|\chi(t)\rangle$ and for $\psi(t)\rangle$, and n forward propagations, where n is the number of steps required to find the maximum value of the functional with respect to the field in the direction of its gradient. Therefore, compared with GM, the Krotov method introduces immediate feedback and requires fewer propagations per iteration.

III. The System

As an illustrative example, we will consider a simple 1D system, a Morse potential with seven bound eigenstates. The Hamiltonian for the system is

$$H = -\frac{\hbar^2}{2\mu}\frac{\partial^2}{\partial x^2} + D\,(1 - \exp(-\beta\Delta x))^2 \qquad (16)$$

with parameters $D = 0.386$ eV (3342.4 cm^{-1}), $\mu = 1$ amu, $x_0 = 2.1$ Å, and $\beta = 2.1$ Å^{-1}. For the discussion of the results below, we give here the characteristic frequencies of the system, ω_{if}, corresponding to the energy gaps between the first four levels: $\omega_{01} = 850$ cm^{-1}, $\omega_{02} = 1550$ cm^{-1}, $\omega_{03} = 2100$ cm^{-1}, and $\omega_{04} = 2400$ cm^{-1}.

We assume a dipole moment coupling with the radiation, and we take the dipole function to have the form

$$\mu = 1 - \exp(-\beta(x - x_0)) \qquad (17)$$

The dipole function coordinate will effectively induce an overall shift of the energy levels at large values of x to higher or lower values, depending on the sign of the field amplitude. The sign of the interaction is chosen so that a negative value of the dc field will cause a decrease in the dissociation barrier. We discard all solutions with optimal field intensities greater than 10^{13} W/cm^2 (i.e., we change the penalty function and start over with the initial guess) since this is above the Keldysh limit and is assumed to lead to atomic ionization.[13]

IV. Results and Discussion

A. Comparison of KM and GM Results. Our goal here will be to compare the Krotov method (KM) and gradient methods (GM), analyzing both the optimal pulses that they generate and the numerical effort they require. For this part of the study we focus on selective excitation of the fourth Morse eigenstate (labeled $|3\rangle$), starting from the ground state (labeled $|0\rangle$).

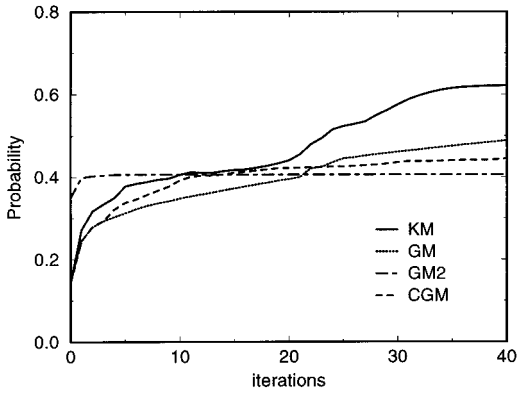

Figure 1. Probability to select the target state $n = 3$ at different iterations for Krotov and gradient methods. The final time is 100 fs. The nomenclature is explained in the text.

In Figure 1, the yield as a function of iteration number is plotted for four different test cases. Three of the tests represent distinct methods—Krotov (KM), gradient line-search method (GM), and conjugate gradient line-search method (CGM)—which were all started with the same initial guess, a Gaussian-shaped pulse with carrier frequency matching the energy gap between states $|0\rangle$ and $|3\rangle$ (ω_{03}). The fourth test (GM2) starts from a Gaussian-shaped pulse whose parameters have been preoptimized. From the plot we observe that the final yield obtained by the Krotov method (0.62) is clearly better than that obtained with the other methods (the best of the others, GM, gives a final yield of 0.49). In this example CGM rises faster than GM, although GM attains a higher ultimate value. The comparison of GM2 with GM suggests that a very efficient guess pulse may lead to fast convergence, but is not guaranteed to attain the highest yield. Both these features are consequences of the initial guess in GM2 being close in function space to a locally optimal pulse. This is the opposite extreme for the KM result, where the initial guess is quite distant in function space from the optimal pulse. In terms of numerical effort there is an even larger advantage to KM, which requires only three wavepacket propagations per iteration, as compared with gradient-based methods, which require many more, due to the line search necessary.

In Figure 2 we analyze the features of the optimal pulses obtained with the different methodologies. The frequency spectrum provides a good measure of the distance between the pulses in the functional space. Recall that the $0 \rightarrow 3$ transition frequency is 2100 cm^{-1}. Therefore, we observe that the GM2 solution just makes use of the direct transition, while, at the opposite extreme, the KM pulse has no component of direct transition. GM is in a middle position, with some component of direct and indirect transitions. The CGM pulse is essentially identical to the GM pulse and is not shown.

To show schematically how the optimal pulses work, we use the energy level diagram for the Morse potential. Figure 3a shows schematically the mechanism exploited by KM. It consists of the coherent superposition of two pathways, each consisting of a two-photon transition. Figure 3b shows schematically the mechanism used by GM. It involves the coherent superposition of three pathways, one being the single-photon direct transition to the final state and the other pathways again

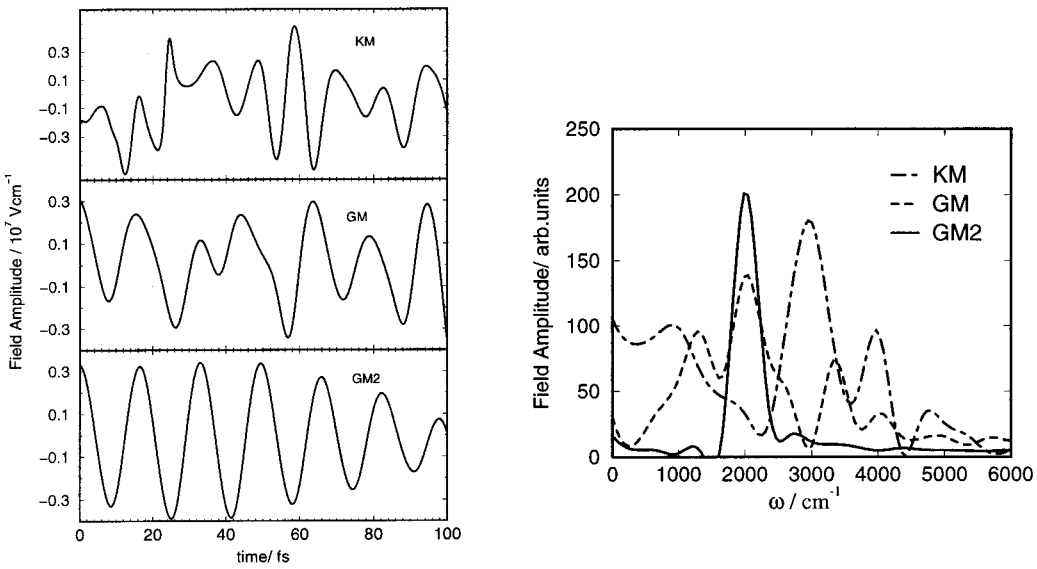

Figure 2. Optimal pulses in time (left) and frequency (right) for KM, GM, and GM2 cases. The direct transition frequency, ω_{03}, is equal to 2100 cm^{-1}.

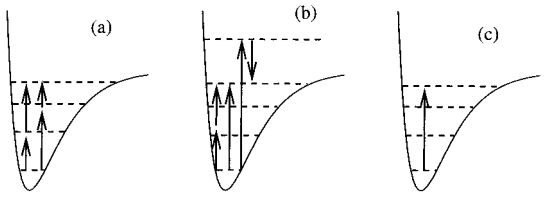

Figure 3. Level diagrams illustrating the main processes participating in the dynamics driven by the KM (a), GM (b), and GM2 (c) pulses. The energy levels represent roughly the Stark-shifted eigenvalues of the Morse potential.

being two-photon, but now with one of these pathways employing a virtual transition through the dissociative continuum. We will refer to this scenario as three-color, because it employs three very different frequencies. Figure 3c shows schematically the mechanism employed by CGM. It is again the single-photon, direct pathway to the final state.

To connect the pictures above and the energy levels of the bare Morse oscillator, it is necessary to take into account the zero-frequency components of the fields, which induce a dc Stark shift. This shift is especially important in the KM solution, where the yield drops to less than one-third (0.19) after filtering this component. The KM solution can be analyzed as a dc component plus a broad band ranging from very low frequencies to almost dissociation and centered around 900 cm^{-1} and plus other strong bands at frequencies higher than the continuum of dissociation. The strong and negative dc component (-1.8×10^7 V/cm) causes a lowering in the energy levels of the potential. We have checked this by diagonalizing the Hamiltonian formed by the potential and the time-independent component of the field coupled by the dipole moment. The first three Stark-shifted fundamental frequencies are $\omega_{01} = 680$ cm^{-1}, $\omega_{02} = 1200$ cm^{-1}, and $\omega_{03} = 1600$ cm^{-1}. The lowering of energy levels implies that the broad spectral band around 900 cm^{-1} overlaps the direct transitions ω_{01}, ω_{02}, ω_{13}, and ω_{23}, shown in Figure 3a. The signature of these transitions is seen in the time dependence of the transition probabilities, shown in Figure 4. The system evolution can be described as sequential, proceeding from $|0\rangle \rightarrow |1\rangle \rightarrow |2\rangle \rightarrow |3\rangle$. To test the importance of direct transitions from $|0\rangle \rightarrow |3\rangle$, the higher frequencies in the spectrum were filtered; the final yield remained almost constant. This implies that the strong band centered around 3000 cm^{-1} is almost not

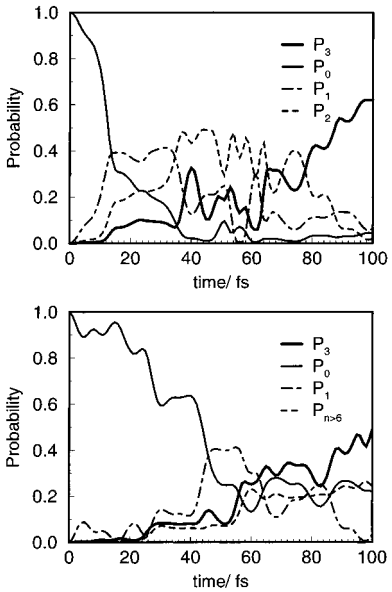

Figure 4. Population histories for the main states involved in the dynamic evolution, for KM (upper) and GM (lower) cases. The target state is $n = 3$.

contributing to the system evolution. The presence of a great number of photons not being used by the optimal field can be explained because the optimization did not penalize strongly the energy fluency of the pulses.

The mechanism of the GM pulse is somewhat more complicated. The direct transition due to the band centered above 2000 cm^{-1} yields around 40% of the objective, the rest being due to the joint effect of the dc component and of the two bands centered at 1300 and 3300 cm^{-1}. The dc component (5.0×10^6 V cm^{-1}) this time *raises* the energy levels (and reduces the strong anharmonicity), allowing the first of the bands to match the energy gap between $|0\rangle$ and $|1\rangle$ within the energy−time resolution of our experiment (the Stark-shifted fundamental frequency for the ω_{01} transition is now 900 cm^{-1} and ω_{13} is approximately 1300 cm^{-1}). Subsequent absorption generates the transition from $|1\rangle \rightarrow |3\rangle$. This route is borne out by the time development of the populations in Figure 4. Nevertheless, the band centered at higher wavelength also plays an important role: filtering out the high-frequency component reduces the

TABLE 1: Probability of Reaching the $n = 4$ Morse Eigenstate at Different Final Times (in Percent)[a]

	150 fs	250 fs	400 fs
optimal pulse	67.0	81.6	85.8
dc filter	25.7	38.0	62.2
low-freq filter	1.0	5.1	54.3
high-freq filter	52.2	73.8	33.5

[a] The yield using the optimal pulse is compared with that obtained after a dc filter, a low-frequency filter (including dc and all frequencies below the direct transition $|0\rangle \rightarrow |4\rangle$), and a high-frequency filter (including the direct transition and above).

yield from 0.49 to 0.34. The high-frequency contribution works by a stimulated Raman process in which there is a transition to a virtual state in the continuum, followed by a downward transition to level $|3\rangle$. That this stimulated process is at work is consistent with the fact that the energy difference between the high-frequency band and the band at 3300 cm^{-1} overlaps ω_{03}. Therefore, the GM mechanism employs three colors, in addition to the dc component.

Finally, for the GM2 case, only the direct transition contributes to the population in the target state.

B. Effect of Changing the Final Time. Having shown that the choice of optimization method can dramatically affect the nature of the optimal pulse, we now show that relatively benign parameters in the definition of the objective can also completely change the nature of the optimal pulse. To keep the size of the study manageable, below we will use only the Krotov methodology. The first parameter we investigate is the choice of final time, T, at which the yield is measured. We choose as our target state $n = 4$. Note that there is a three-photon resonance in the system, since $\omega_{04} = 3\omega_{01}$, and therefore by choosing the objective as $n = 4$ we put into competition the single-photon and the multiphoton routes. As will be seen below, the relative contributions of the two routes are a strong function of pulse duration and therefore of the optimization parameter, T.

In Table 1 we show the yields obtained for time durations $T = 150$, 250, and 400 fs. It is clear that larger values of T lead to larger yields. This difference is not only quantitative but it is qualitative, in the sense that there is a changeover in mechanism as the final time is increased. As a first indication of this changeover in mechanism, we show in Table 1 the result of applying three different spectral filters to the pulses: (i) filtering the dc, (ii) filtering all low-frequency components (LF) (including the dc and ω_{01}), and (iii) filtering the high-frequency components (HF) (including ω_{04} and all frequencies above direct photodissociation). Since LF and HF give almost a complete partitioning of the pulse spectrum, we associate the yield obtained using the LF with the single-photon route to the objective, while we associate the HF yield with the multiphoton contribution. Moreover, we can interpret the difference in yield between the full optimal pulse and the sum of LF and HF yields as being due to quantum interference between the two routes.

Figure 5 shows the optimal pulses obtained, both in time and frequency, for different choices of T. The pulses associated with the different values of T each work by a different mechanism, as shown schematically in Figure 6. For $T = 150$ fs the main features of the optimal pulse in the frequency domain are a very strong dc component (-2.2×10^7 V cm^{-1}) and two wide bands centered around ω_{01} and ω_{02} (where the frequencies refer to intervals between the dc Stark-shifted Morse eigenstates, not the bare eigenstates). These frequency components are responsible for simultaneous transitions between the state $|0\rangle$ and the states $|1\rangle$ and $|2\rangle$, as seen in Figure 6a. Subsequently,

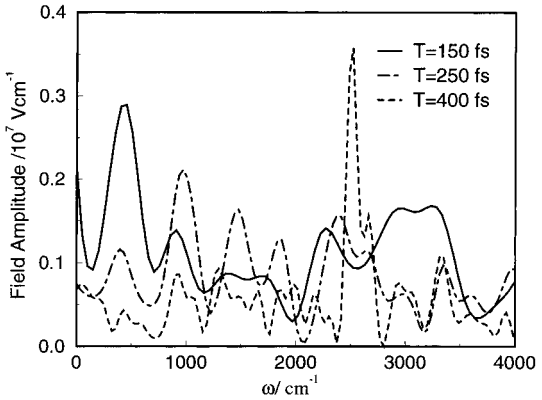

Figure 5. Optimal pulses in frequency domain for state $n = 4$ selection at different final times (T). The frequency for the direct transition is $\omega_{04} = 2400$ cm^{-1}.

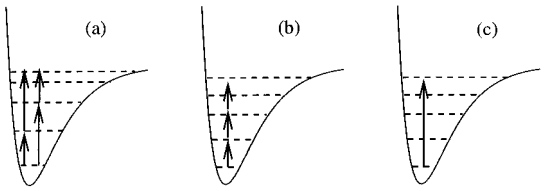

Figure 6. Level diagrams illustrating the main processes participating in the $T = 150$ fs (a), $T = 250$ fs (b), and $T = 400$ fs (c) cases. The energy levels correspond roughly to the Stark-shifted eigenvalues of the Morse potential.

the transitions $|1\rangle \rightarrow |4\rangle$ and $|2\rangle \rightarrow |4\rangle$ are induced to reach the final target. Note that the frequency components conspire to bypass level $|3\rangle$. The resonance between the field frequencies and these transition intervals again requires taking into account the dc Stark shift. It is striking that the 150 fs solution does not exploit either the one-photon or the three-photon resonances, but uses two superposing sets of two-photon transitions.

For $T = 250$ fs the dc component is low and positive (5.9×10^6 V/cm), thereby reducing the anharmonicity of the system. In addition, there are frequency components at $|0\rangle \rightarrow |1\rangle$, $|0\rangle \rightarrow |2\rangle$, $|0\rangle \rightarrow |3\rangle$, etc. However, by far the most important of these frequencies is the $|0\rangle \rightarrow |1\rangle$. The dc component acts to enhance the resonance of the three-photon pathway $|0\rangle \rightarrow |1\rangle \rightarrow |2\rangle \rightarrow |4\rangle$, so that only the $|0\rangle \rightarrow |1\rangle$ frequency is necessary for the process. (Note that, although the concept of a resonance condition is of limited utility for extremely short times, by times on the order of $T = 250$ fs and $T = 400$ fs the resonance condition plays a significant role.) Filtering the dc component eliminates the resonance with the intermediate state $|2\rangle$, reducing the yield to less than one-half. In contrast, the direct single-photon route is responsible for less than 10% of the total yield.

Finally, in the case $T = 400$ fs, the direct single-photon route is responsible for 60% of the yield, while all the multiphoton routes combined are responsible for only 40% of the yield. For comparison, note that even a simple CW pulse can transfer 72% of the system's population from $|0\rangle \rightarrow |4\rangle$.

Additional support for this changeover in mechanism as T is increased is shown in Figure 7, where the transition from simultaneous multiphoton pathways ($T = 150$ fs) to a single sequential multiphoton ($T = 250$ fs) to a direct transition ($T = 400$ fs) is seen clearly in the behavior of the population histories.

C. Effect of Changing the Functional Form. The focus of the study will now turn to multiphoton dissociation dynamics. In the spirit of the present methodological survey, we will explore the effect on the optimal pulses of the choice of the projector that is used to define dissociation. We have devised

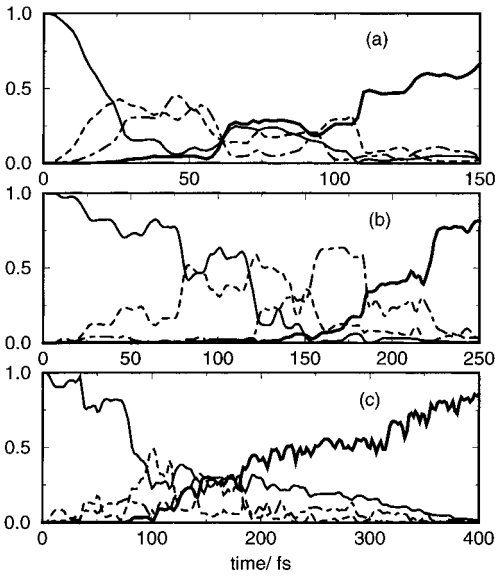

Figure 7. Population histories in the optimal dynamics for selecting the $n = 4$ state, for $T = 150$ fs (upper), $T = 250$ fs (middle), and $T = 400$ fs (lower). The solid line represents the initial state, $n = 0$, and the thicker line the target state, $n = 4$. The most representative intermediate states are $n = 1$ (dashed line) and $n = 2$ (dashed-dot line).

two different projectors that in principle represent the system bond breaking. The first is a scattering states projector, which we call P_s, mathematically defined as

$$P_s \equiv 1 - \sum_{i=0}^{6} |\phi_i\rangle\langle\phi_i| \tag{18}$$

and the second is an asymptotic coordinate projector (P_x) defined as

$$P_x \equiv \int_{x \geq x_{asymp}} dx |x\rangle\langle x| \tag{19}$$

For numerical reasons, when applying P_x, we filter negative momentum components, although this accounts for only a small percentage of the amplitude. The final time used in these calculations is 100 fs, and the initial guess pulse is Gaussian-shaped. The initial guess produces 27.5% dissociation, defined using the scattering projector. We use KM for the subsequent optimization.

The optimal pulse obtained using the scattering projector gives a value of the objective, J_{P_s}, of 0.77 after 12 iterations, while the optimal pulse obtained using the coordinate projector gives a value of the objective, J_{P_x}, of 0.85 after only 6 iterations. The main features of the P_s pulse are a low negative dc and a wide band peaking at ω_{02} and ω_{03}. The main components of the P_x pulse are a high positive dc and a band centered at ω_{01}. Figure 8 shows the optimal pulses in the time and frequency domains. Note that in the P_x case the majority of the photons are concentrated in a very short time interval around 40 fs. (Figure 8, bottom left). The strange features of the shape in this interval are due to the higher frequency components of the field. Filtering these frequencies (Figure 8, middle left) has almost no effect on the dissociation yield. The part of the pulse which remains after filtering essentially works as a hammer, synchronized with the arrival of the wavepacket at the inner turning point of the potential. Evidence for this mechanism will be given below.

As before, we analyze through time-dependent observables the mechanism by which the pulses act on the system. In Figure 9 we show the population histories for the most important states. In the P_s case, we see evidence for a two-step process: a first step in which the photons simultaneously transfer population to the intermediate excited states $|1\rangle$, $|2\rangle$, and $|3\rangle$ and a second step (in the last 20 fs) in which the bond is impulsively broken. In the P_x case we have instead only a single impulsive absorption of energy that transfers population rapidly (in about 10 fs) and successively to all excited bound states and finally dissociates. For the photodissociation problem it is fruitful to follow the wavepacket dynamics in the coordinate frame, as well as in the eigenstate frame. Figure 10 shows the time evolution of the wavepackets, for both the P_s and the P_x cases. We superimpose the shape of the potential surface to facilitate the view of the wavepacket oscillating between the inner and the outer wall of the potential, although the ordinate represents the time and not the energy expectation value of the system. Indeed, the height of the potential curve in each plot is scaled to the expectation value of the energy at the final time.

In both the P_s and P_x cases the bands are so broad that the concept of resonance is of limited value in understanding the

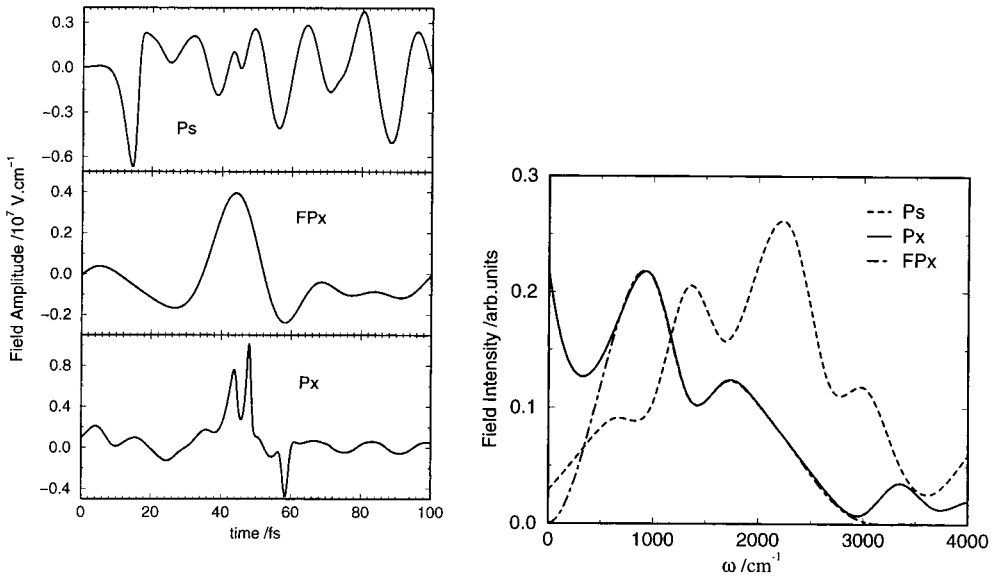

Figure 8. Optimal pulses in time (left) and frequency (right) domain for the P_s and P_x cases. Also shown is the pulse obtained after filtering the dc component and the above threshold frequencies of the P_x pulse (labeled *FPx*).

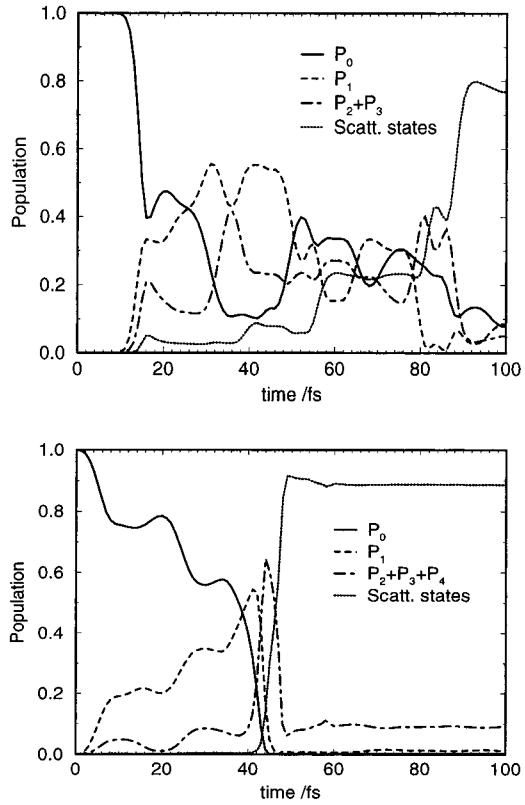

Figure 9. Population histories for the main states implied in the dynamic evolution, for P_s (upper) and P_x (lower) cases.

mechanisms at work. Nevertheless we can infer from the position of the main bands in the pulses, together with the energy expectation value vs time, a rough measure of the number of photons absorbed and their time of absorption. By correlating the evolution of the wavepackets in the coordinate representation with the energy history of the system (see Figure 11), we can infer not only when the photon is absorbed but also what it is being used for. In the P_s case the bands are blue-shifted relative to the P_x case (see Figure 8). The spectral features around 2000 cm^{-1} produce a coherent excitation of levels $|2\rangle$ and $|3\rangle$ via a one-photon process. A second photon gives the final impulse during the "collision" with the potential inner wall, as seen in the left part of Figure 10. In the P_x case the spectrum is farther to the red; however, the final amount of energy absorbed is higher. Therefore, it is clear that a greater number of photons are taking part in the photodissociation process. In fact, we estimate that more than five photons are absorbed right before, during, and after the collision of the wavepacket with the inner wall of the Morse potential (Figures 9 lower and 10 right).

Although not shown in Figure 8, there are high-frequency components in the spectrum that are clearly above the threshold for direct dissociation. These highly energetic photons give a strong impulse to the wavepacket, creating some high-momentum components which reach the asymptotic region within time *T*. If these high-frequency components are filtered, the objective drops from 89% to 67%. Recall that in the P_x case the objective is defined in terms of the portion of the wavepacket that crosses the asymptotic coordinate in time *T*. Thus, this drop is to some extent an artifact of the definition of the objective: if the same pulse is used but the objective is defined in terms of projection onto the scattering states, there is almost no drop in yield.

The role of the dc component is very different in the P_s and P_x cases. In the P_s case, the dc component is low and negative (-3.0×10^6 V/cm), and therefore it reduces the dissociation energy and increases the anharmonicity of the potential. This in turn increases the complexity of the nodal structure of the wavepacket, which ultimately reflects itself in a more complicated momentum distribution of the fragments (see Figure 12). In the P_x case, the dc component is high and positive (2.3×10^7 V/cm), so it reduces the wavepacket distortion and more importantly it reduces the time for the first collision of the wavepacket with the inner turning point of the Morse potential. This reduction in time, in turn, reduces the time necessary for the wavepacket to reach the asymptotic region, increasing the objective. If the dc component is filtered, the asymptotic amplitude decreases significantly, not only because the wavepacket requires more time to reach the inner turning point of the potential but also because it is slightly desynchronized, when it reaches the inner wall of the potential, from the most intense part of the pulse, at 40 fs. The second effect will also lead to a significant decrease in the ultimate dissociation yield (i.e., the overlap with the scattering states), although the first effect will not.

In the P_x optimal dynamics, the wavepacket stays compact until after dissociating, and thus the final momentum distribution

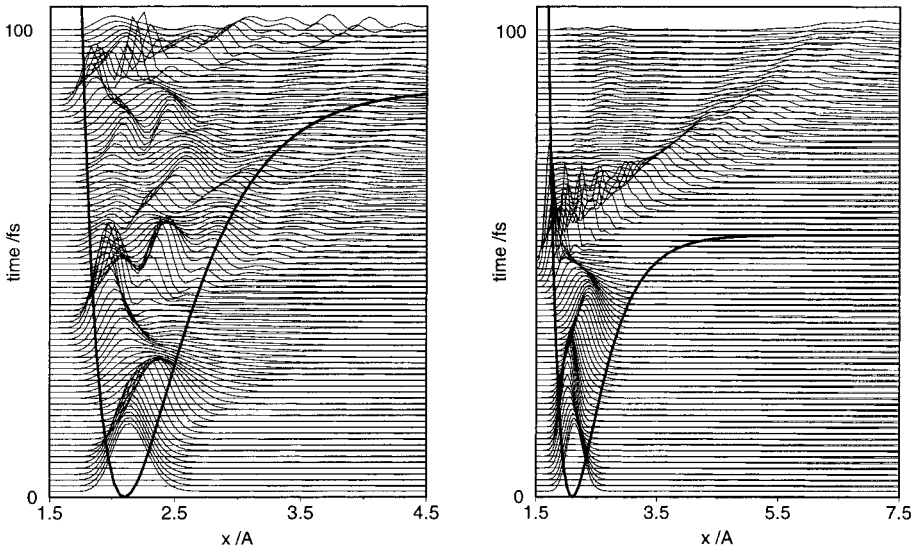

Figure 10. Time evolution of the wavepackets for the P_s (left) and P_x (right) cases. We superimpose the potential curve to facilitate the view of the dynamics, but the ordinate represents the time coordinate and not the expectation energy of the system. For more explanations see the text.

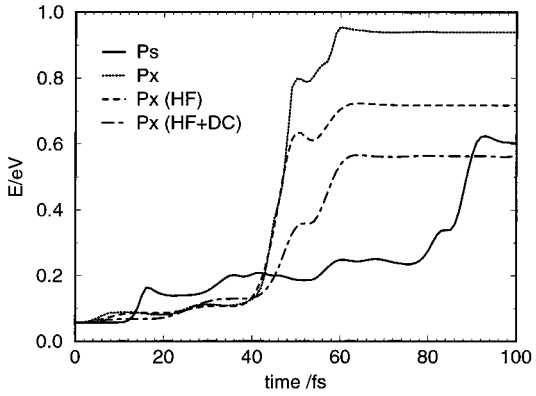

Figure 11. Expectation value of the system energy as a function of time for the P_s and P_x cases. The high absorption of energy in the P_x case can be reduced by filtering the high-frequency components of the field (as shown in the case labeled HF) and also the dc components of the field (shown in the case labeled dc).

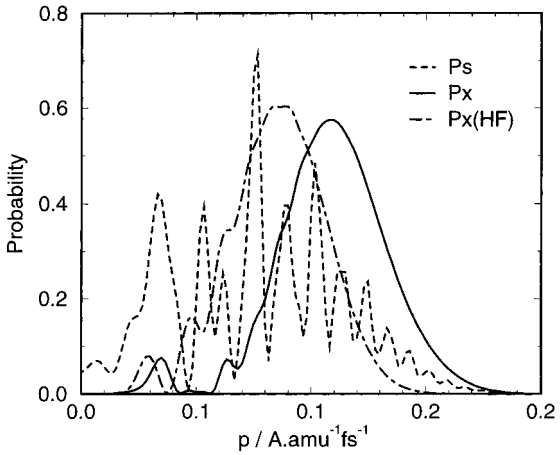

Figure 12. Final momentum distribution for the P_s and P_x cases. SP is shifted to lower values of momentum and exhibits nodal structure in comparison with P_x. Filtering the high-frequency components that are present in P_x induces a shift to lower values of momentum in the momentum distribution of the fragments at final time. This is shown in the curve labeled P_x (HF).

is structureless; this is in marked contrast with the P_s case, where the momentum distribution is highly structured. Eliminating the dc component of the P_x excitation increases the effective anharmonicity and leads to a structured momentum distribution as in the P_s case. Moreover, the P_x momentum distribution is centered at higher values than the P_s case, as a result of the high-frequency components of the excitation and the synchronization of the pulse with the collision at the inner wall of the potential discussed above. Eliminating the high-frequency components (above direct dissociation) shifts the momentum distribution to lower values but does not effect the nodal structure (see Figure 12).

In closing this section on numerical results, we make some general observations on the optimal pulses we obtained. In all our simulations the underlying structures of the optimal pulses are more easily interpreted in the frequency domain than in the time domain. In all situations explored we can describe our pulses as a sum of a time-independent electric field and a set of Gaussian-shaped pulses (ranging from one to three in the most complex case) of different colors. Husimi plots of the pulses (not shown) indicate that the pulses are unchirped and that the different colors operate essentially at the same time. Of course, our findings may be particular to the model chosen, which consists of a shallow Morse potential, as well as our choice of dipole function.

V. Summary and Conclusions

Optimal control methods have become a popular tool in quantum dynamics calculations, and we expect their use to eventually become routine in the world of experimental laser chemistry. In this article we have attempted to show that OCT is not a black box that provides just one answer to a given problem, but on the contrary, by manipulating the different parameters and definitions available in OCT, a variety of "optimal" pulses can be devised, depending on the needs or requirements of the experimental designs. Moreover, even when the experimental realization of these pulses is not completely possible, the understanding of the underlying structure of the optimal field may provide insight into the physical processes that guide the system to the desired objective.

We tested here the effect of (1) the choice of optimization methodology, (2) the choice of final time, and (3) the choice of the objective functional chosen on the type of solutions obtained in OCT. In a future paper we plan to discuss the effect on the optimal pulses of changing the constraints on a small set of experimentally controlled parameters.[14] We have seen that KM is less time consuming than GM because it makes possible large changes in the electric field at successive iterations and because it requires fewer operations per iteration. This ability to search for distant solutions in the space of the pulses makes KM especially powerful when the initially guessed pulse is far from the optimal one, i.e., when intuition fails. However, more important in the context of the present study is that the GM methods can get trapped near the initial guess, while the KM method quickly escapes from the region of the initial guess.

In the selective excitation of Morse bound states we have seen a clear changeover in mechanism as the definition of the final time T is changed. For $T < 400$ fs we found a preference for multiphoton (two or three photon) routes, while if $T \geq 400$ fs the mechanism changes to single-photon excitation.

In the photodissociation problem we have tested how the functional form of the objective affects the solutions. We observed that when we use a coordinate projector (P_x), the optimal pulse forces a vertical plus horizontal displacement of the wave function and therefore favors faster energy absorption and hotter translational distributions. In contrast, using a scattering projector (P_s) the driven wavepacket experiences only a vertical displacement (the asymptotic part of the wavepacket at $T = 100$ fs is less than 6%). Moreover, due to the sign of the dc Stark shift, the momentum distribution is wider and exhibits nodal structure. The P_s dissociation case is more "economic" in that it requires less intense fields and fewer photons are absorbed. It is also physically more meaningful, since amplitude in these states will reach dissociation, even if they are not there at the final time T. However, the use of a scattering projector is more cumbersome computationally, since the system-bound states need to be calculated.

Finally, we have observed that by changing the high-frequency or the dc components of the optimal pulses we can change the translational distribution of the fragments. We therefore expect that by manipulating these components of the pulses some degree of momentum selectivity can be achieved. This idea is currently being tested.

The present study therefore indicates that the "optimal" solution is largely in the eye of the beholder, i.e., in the way the researcher defines the parameters of the objective. Moreover, there are other important parameters, e.g., robustness,

which we have not even been able to touch on in this study. The ambiguity in the definition of optimal solutions may be viewed as a shortcoming of the approach, but alternatively it may be viewed as giving the method extra flexibility. Although the present study was for a simple model potential, we believe that the flexibility in the definition of the optimal solution applies also to more complex systems.

References and Notes

(1) Potter, E.; Herek, J. L.; Pedersen, S.; Liu, Q.; Zewail, A. H. *Nature* **1992**, *355*, 66.

(2) Scherer, N. F.; Ruggiero, A. J.; Du, M.; Fleming, G. R. *J. Chem. Phys.* **1990**, *93*, 856.

(3) Weiner, A. M.; Heritage, J. P.; Thurston, R. N. *Opt. Lett.* **1986**, *11*, 153.

(4) Weiner, A. M.; Leaird, D. E.; Wiederecht, G. P.; Nelson, K. A. *Science* **1990**, *247*, 1317.

(5) Shnitman, A.; Sofer, I.; Golub, I.; Yogev, A.; Shapiro, M.; Chen, Z.; Brumer, P. *Phys. Rev. Lett.* **1996**, *76*, 2886.

(6) Bardeen, C. J.; Cao, J.; Wilson, K.R. Submitted to *J. Phys. Chem.*

(7) Paramonov, G. K.; Savva, V. A. *Phys. Lett. A* **1983**, *97*, 340. Combariza, J. E.; Just, B; Manz, J.; Paramonov, G. K. *J. Phys. Chem.* **1991**, *95*, 10351. Dibble, B. G.; Shirts, R. B. *J. Chem. Phys.* **1991**, *94*, 3451.

(8) Chelkowski, S.; Bandrauk, A. D.; Corkum, P. B. *Phys. Rev. Lett.* **1990**, *65*, 2355.

(9) Dahleh, M.; Peirce, P. A.; Rabitz, H. *Phys. Rev. A* **1990**, *42*, 1065.

(10) Kosloff, R.; Rice, S. A.; Gaspard, P.; Tersigni, T.; Tannor, D. J. *Chem. Phys.* **1989**, *139*, 201.

(11) Tannor, D. J.; Kazakov, V. A.; Orlov, V. In *Time Dependent Quantum Molecular Mechanics*; Broeckhove, J., Lathouwers, L., Eds.; Plenum Press: NewYork, 1992.

(12) Krotov, V. F.; Fel'dman, I. N. *Eng. Cybern.* **1984**, *21*, 123.

(13) Dietrich, P.; Corkum, P. B. *J. Chem. Phys.* **1992**, *97*, 3187.

(14) Sola, I. R.; Muñoz-Sanz, R.; Santamaria, J. Contribution sent to the special Femtochemistry issue, *J. Phys. Chem. A.*